JOURNAL OF MATERIALS SCIENCE 35 (2000) 1097–1103

Fabrication of nanoporous single crystal mica templates for electrochemical deposition of nanowire arrays

L. SUN*, C. L. CHIEN‡, P. C. SEARSON*
*Department of Materials Science and Engineering and ‡Department of Physics and Astronomy, The Johns Hopkins University, Baltimore, MD 21218, USA
E-mail: searson@jhu.edu

Nanopores with lateral dimensions as small as 33 nm have been fabricated by nuclear track etching in 5 μm thick, single crystal mica wafers. The nanopores have a diamond shape with their axes aligned with the crystal axes of mica as a result of anisotropic etching. Nickel nanowire arrays with a constant volume fraction have been fabricated by electrodeposition into the nanopores. The magnetic properties of the nickel nanowire arrays in the mica templates are reported.

1. Introduction

Electrodeposition of metals into porous templates has been used as a method to fabricate a wide range of quasi-one-dimensional nanostructures [1–12]. Anisotropic magnetic properties have been reported in ferromagnetic [6–9] and multilayer [10–12] nanowires. Templates for electrochemical deposition of nanowire arrays include etched nuclear particle tracks [13–17], porous alumina films formed by anodic oxidation of aluminum [18–20], and nanochannel glass films [21]. The intrinsic properties of nanowire arrays are directly related to the properties of the nanoporous template such as the relative pore orientations in the assembly, the pore size distribution, and the surface roughness of the pores.

Nuclear damage tracks in dielectric materials are created by the passage of high energy particles. Along the trajectory of the particles, the so-called Coulomb explosion phenomenon gives rise to regions of local structural disorder such as point defects in crystals and bond breaking in polymers [16, 17, 22]. Due to the local disorder, the chemical activity of the damage tracks is much higher than the bulk material. In the presence of a suitable etchant, the etch rate of the damage tracks may be several orders of magnitude higher than the bulk material so that the damage tracks can be etched to form an array of uniform parallel sided pores. Further etching results in enlargement of the pores at a rate determined by the bulk etch rate. The area density of pores is determined by the fluence of the particles and the pore size is determined by the etching time. Nuclear track etching has been widely used in particle identification, fission track dating, and filtration [16].

The electrochemical deposition of nanowire arrays was first reported by Possin [1, 2] who deposited tin nanowires in tracked mica films. Subsequently Giordano and coworkers studied electron localization effects in gold and platinum nanowires [3, 4]. However, these reports did not include any details of the structural and morphological properties of the nanowires. Most recent work has focussed on nanowire arrays fabricated in tracked polycarbonate membranes [6–12, 23]. However, polymer membranes are not ideal since the internal surface of the pores can be quite rough [24]. The polymer membranes are also relatively soft so that characterization of the pore morphology and distribution by force microscopy is not straightforward. Further limitations associated with commercially available membranes are the high pore density and the large angle between the pore axis and the surface normal (as high as 30°), which can greatly reduce the shape anisotropy [8].

Here we report on the fabrication and characterization of nanoporous templates in single crystal mica wafers. The pores are diamond-shaped with well defined crystal axes that are related to the crystal structure of the mica. We show that the coercivity and squareness of nickel nanowire arrays in mica films are significantly enhanced compared to nanowires of the same dimension formed in polycarbonate membranes. Furthermore, we show that the Curie temperature of nickel nanowire arrays in mica films is dependent on wire diameter and follows finite size scaling theory.

2. Experimental

The nanporous templates were fabricated by etching particle tracks in 5 μm thick single crystal muscovite mica wafers (Spruce Pine Co). Particle tracks were created by exposure to approximately 6 MeV α particles from a 100 μCi Cf^{252} source (Isotope Products) in a chamber at a base pressure of about 10^{-3} Torr. The particle tracks were collimated to within 5° by locating the mica wafers 1.9 cm from the source. The track depth

for 6 MeV α particles in mica was determined to be 9.7 μm, consistent with an energy deposition of 11–12 MeV cm^{-2} mg^{-1} for mica [25].

The particle tracks were etched by immersing the irradiated wafers in 20 wt.% HF (11.4 M). The etching process was performed in a two compartment cell and was monitored by measuring the resistance across the mica wafer using platinum wires located in each compartment of the cell. The shape, density, orientation, and uniformity of the pores in the mica films were examined by scanning electron microscopy and atomic force microscopy (AFM, Topometrix). The orientation of the pores with respect to the mica lattice was determined by X-ray measurements performed on a four circle diffractometer (Philips X'Pert MRD).

Nickel nanowire arrays were fabricated by electrochemical deposition into the porous films. The working electrode was provided by a gold layer sputter deposited onto one side of the wafer. In order to ensure that the gold layer was continuous, the thickness was about three times the pore diameter. Nickel was deposited from a solution of 20 $g\,l^{-1}$ $NiCl_2 \cdot 6H_2O$, 515 $g\,l^{-1}$ $Ni(H_2NSO_3)_2 \cdot 4H_2O$), 20 $g\,l^{-1}$ H_3BO_3 buffered to pH 3.4 at a potential of -1.0 V (Ag/AgCl). The experimental details have been described elsewhere [4]. The magnetic properties of the nickel nanowire arrays were determined using a vibrating sample magnetometer.

3. Results and discussion

Fig. 1 shows a plan view scanning electron microscope image of an irradiated and etched mica film. The pores are diamond in shape with characteristic angles of 60° and 120° respectively, and are oriented with respect to each other. The well defined corners indicate that the etching of mica in HF is highly anisotropic [26]. For convenience, we define the effective pore diameter as the diameter of the circle with the same area as the diamond shaped pore. Fig. 2 shows a scanning electron microscope image of an irradiated and etched mica film sectioned to reveal the interior of the pores. It is evident that the pore axes are parallel and that the interior surfaces of the pores are smooth and free from etching residues. The uniformity of the pores throughout the thickness of the film shows that the etch rate for the damage tracks is much faster than the bulk etch rate.

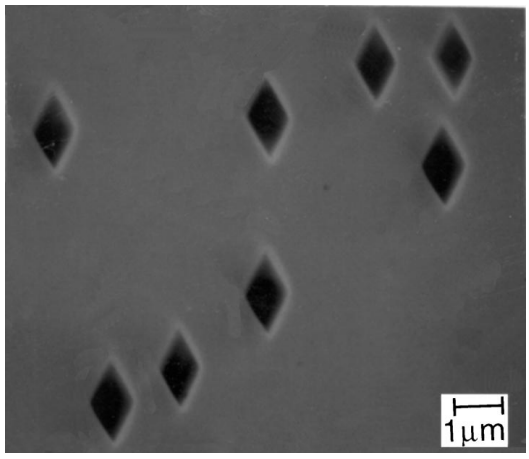

Figure 1 Scanning electron microscope plan view image of etched particle tracks in single crystal mica.

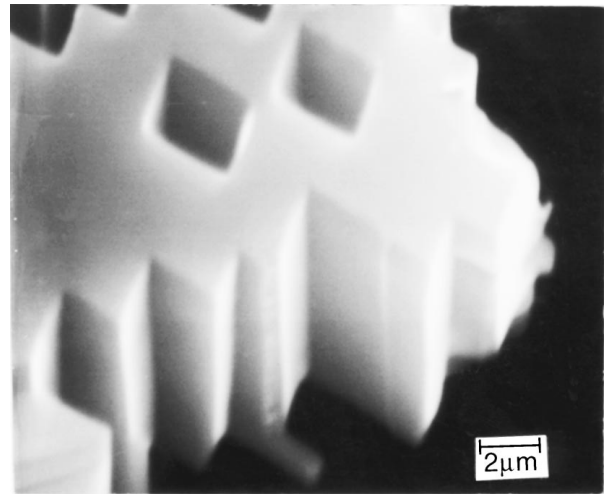

Figure 2 Scanning electron microscope cross-sectional image of 2.3 μm pores in mica.

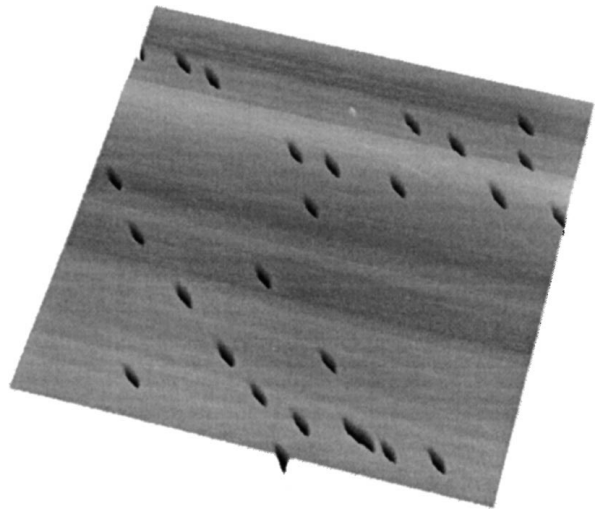

Figure 3 2 μm × 2μm AFM image showing 50 nm nanopores in a single-crystal mica film.

Fig. 3 shows a contact mode AFM image of the surface of the mica film with 50 nm pores and a density of 1×10^9 cm^{-2}. This image shows that the nanopores have the same shape, size, and orientation. The pores are randomly distributed as expected from the stochastic nature of the irradiation process. Images from both sides of the mica wafers after etching were identical, with no observable differences in pore size, pore density, pore shape, and orientation.

The density of particle tracks in the mica films, inferred from the pore density, is proportional to the irradiation time, as shown in Fig. 4. The slope of the line corresponds to a track generation rate of 1.27×10^3 cm^{-2} s^{-1}. Since the half-life of californium is 2.73 years, we note that the track generation rate decreases with time. For experiments reported here, irradiation times of 5×10^4 to 2×10^6 s were used to obtain pore densities between 5×10^7 and 2×10^9 cm^{-2}. Since the fraction of overlapping pores is low (see below) the pore density is essentially the same as the track density.

The etching process and evolution of the pore morphology was monitored using electrical resistance

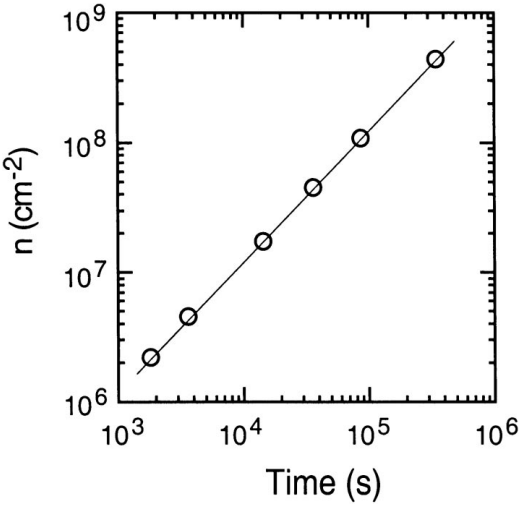

Figure 4 Pore density obtained from SEM images versus irradiation time.

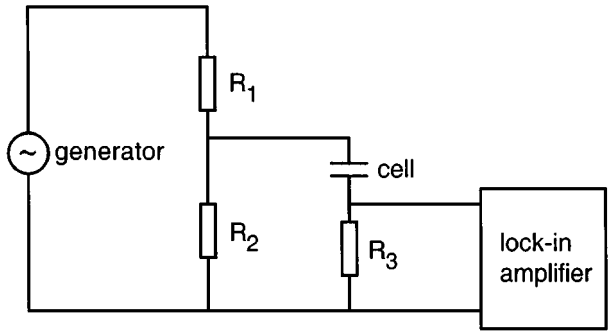

Figure 5 Circuit for measurement of the cell resistance. For measurements reported here, $R_1 = 600\,\Omega$, $R_2 = 5\,\Omega$, $R_3 = 46.9\,\Omega$. The measurements were performed using an ac voltage of 4 V at a frequency of 10 kHz.

measurements. The time dependent resistance $R(t)$ is given by:

$$R(t) = R_0 + \frac{\rho l}{\pi n A r^2} \qquad (1)$$

where R_0 is the series resistance of the cell and is dependent on cell geometry, ρ is the resistivity of the solution, l is the thickness of the tracked film, A is the irradiated area, n is the pore density, and r is the pore radius. The circuit used to measure the resistance of the etching cell is shown in Fig. 5. From measurements without a film in the cell, R_0 was determined to be 20.32 Ω for 20 wt.%HF (11.4 M). The average pore size can then be determined from the measured resistance taking $\rho = 4.7\,\Omega$ cm for the etchant, $A = 0.2025$ cm^2, $l = 5\,\mu$m, and using the pore density determined from the irradiation time. Fig. 6 shows a plot of pore diameter versus etching time obtained from the measured resistance for a track density of 8.0×10^6 cm^{-2}. The breakthrough time was typically 20–22 seconds for the 5 μm thick mica films, corresponding to an etch rate for the damage tracks of 1136–1250 Å s^{-1}. The slope in Fig. 7 corresponds to a lateral etch rate of 0.35 Å s^{-1}. Values of about 0.6 Å s^{-1} have been reported in the literature for etching of mica in 20 wt.% HF at 25°C [14, 27]. The slightly lower values obtained here are

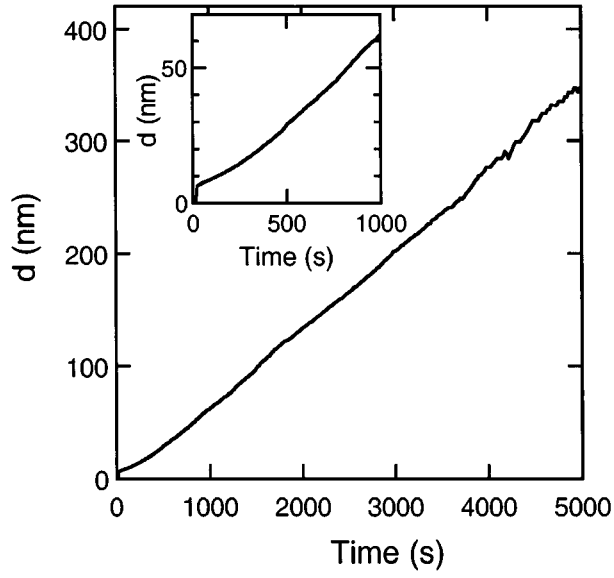

Figure 6 The effective pore diameter obtained from resistance measurements versus etching time. The effective pore diameter is defined as the diameter of a circle having the same area as the diamond shaped pore.

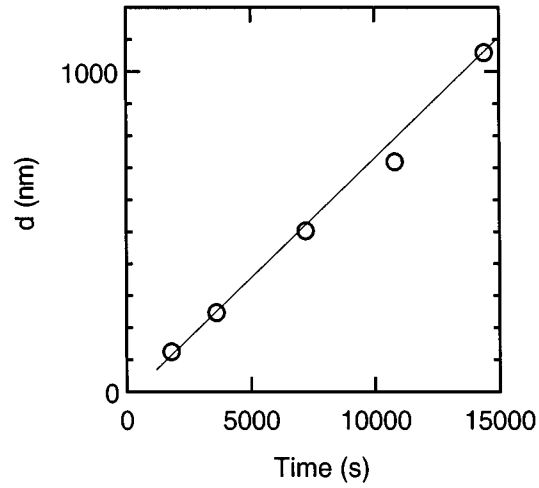

Figure 7 The effective pore diameter obtained from scanning electron microscope images versus etching time.

probably due to the lower temperature used for etching (about 20°C). We note that the vertical etch rate of the bulk material normal to the cleavage plane (i.e. in the [001] direction) is effectively zero [17]. From the ratio of the etch rates (about 3×10^3) the taper of the pore walls is determined to be 0.02°.

Fig. 7 shows a plot of the pore size for longer etching times obtained from scanning electron microscope images. From this Figure it can be seen that there is good agreement between the pore size determined from the resistance measurements and from the scanning electron microscope images, resulting in the same value for the lateral etch rate.

The shape of the pores in the mica films is due to the anisotropy in the in-plane etch rates, originating from the crystal structure of the mica. X-ray diffraction patterns obtained from mica powder prepared by grinding the wafers confirmed the monoclinic structure with the expected lattice parameters ($a_1 = 5.18$ Å, $a_2 = 9.02$ Å, $a_3 = 10.02$ Å, $\alpha = \gamma = 90°$, $\beta = 95.5°$) [28–30].

X-ray $\theta/2\theta$ diffraction of the single crystal mica wafers revealed only the (00n) peaks, indicating that the cleavage surface is the (001) plane. The unit cell projection on the (001) cleavage plane has a rectangular structure with in-plane lattice vectors $\boldsymbol{a}_1$ and $\boldsymbol{a}_2$. By performing x-ray ϕ scans we can measure the angular dependence of the projections of diffraction vectors which are tilted from the surface normal with an angle Ψ, and hence we can determine the orientations of the in-plane lattice vectors in reciprocal space $\boldsymbol{b}_1$ and $\boldsymbol{b}_2$. For the monoclinic mica lattice we have $\boldsymbol{a}_1 // \boldsymbol{b}_1$ and $\boldsymbol{a}_2 // \boldsymbol{b}_2$. Thus by comparing the lattice vectors with images of the pores, we can determine the crystal orientation of the pore walls.

Fig. 8a shows three sets of ϕ-scans from the {112}, {$\bar{1}$12} and {023} planes superimposed on the same plot. For the monoclinic structure of mica, the (112) and (1$\bar{1}$2), ($\bar{1}$12) and ($\bar{1}\bar{1}$2), (023) and (02$\bar{3}$) planes have the same 2θ and Ψ values, as can be seen in Table I. Since the in-plane projections of the these planes are very close to the [110], [1$\bar{1}$0], [$\bar{1}$10], [$\bar{1}\bar{1}$0], [010] and [0$\bar{1}$0] directions in reciprocal space, we can determine the orientations of the reciprocal lattice vectors $\boldsymbol{b}_1$ and $\boldsymbol{b}_2$, and hence the $\boldsymbol{a}_1$ and $\boldsymbol{a}_2$ directions in the sample. Comparison of the lattice vectors $\boldsymbol{a}_1$ and $\boldsymbol{a}_2$ with images of the etched pores reveals that the pore walls are parallel to the {110} planes in the mica lattice, as shown in Fig. 8b. The pore walls correspond to the oxygen terminated planes as illustrated in Fig. 9, indicating that these are the slowest etching planes, very similar to the etching process in SiO_2. The 60° angle of the diamond-shaped pores determined from SEM and AFM images is very close to the angle of 59.7° of the diamond enclosed by $a_1 = 5.18$ Å and $a_2 = 9.02$ Å.

TABLE I Measured ϕ angles for the {112}, {$\bar{1}$12} and {023} planes

Plane	2θ	Ψ	ϕ_{meas}
($\bar{1}$12)	27.8681	45.45	85.4
(1$\bar{1}\bar{1}$2)	25.6112	50.74	205.54
(1$\bar{1}$2)	25.6112	50.74	265.4
(1$\bar{1}$2)	27.8681	45.45	25.46
(023)	33.4856	36.4	145.42
(0$\bar{2}$3)	33.4856	36.4	325.20

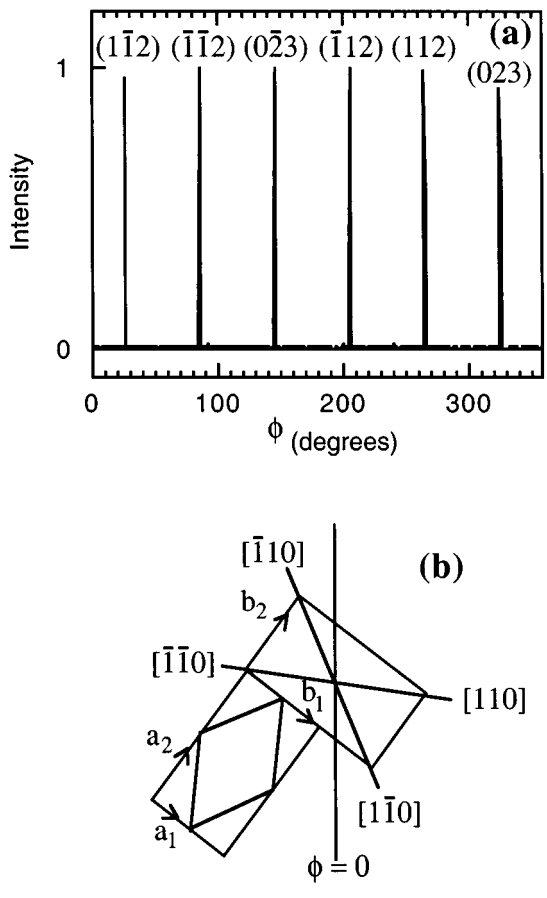

Figure 8 (a) X-ray ϕ-scans of {112} {$\bar{1}$12}, and {023} peaks of mica single crystal film. (b) Crystal vectors ($\boldsymbol{a}_1$ and $\boldsymbol{a}_2$), reciprocal lattice vectors ($\boldsymbol{b}_1$ and $\boldsymbol{b}_2$), and reciprocal vectors [$\bar{1}$ 1 0], [1 $\bar{1}$0], [110], and [1 $\bar{1}$ 0].

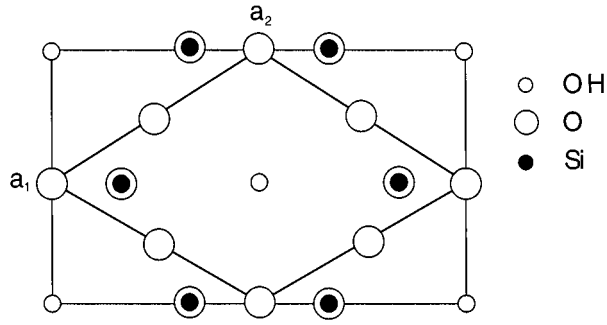

Figure 9 Projection of the atomic arrangement in the (001) plane of mica illustrating that the pore walls correspond to the oxygen terminated planes in the mica lattice.

In making measurements of the properties of nanowire arrays that are a function of pore diameter, pore overlap is an important issue since pores derived from multiple tracks result in a fraction of nanowires with much larger effective diameter than of an isolated pore. For measurements that are dependent on the volume of material it is usually necessary to have a large volume fraction of pores. However, the fraction of overlapping pores increases with increasing volume fraction so that the measurement may be significantly influenced by the fraction of double and triple pores. The fraction of overlapping pores can be approximated by [27]:

$$\frac{m(q)}{n_t} = \frac{(4f)^{q-1}}{q!}\left(1 - 4f + 8f^2 - \frac{32}{3}f^3 + \cdots\right) \quad (2)$$

where $m(q)$ is the number of pores derived from q particle tracks, n_t is the track density, f is the area fraction of pores assuming all single pores. Fig. 10 shows a plot of the fraction of double and triple pores versus the volume fraction f. From this Figure it can be seen that the fraction of double pores is 1% at a volume fraction of about 0.005 and increases to 10% at a volume fraction of 0.07. This clearly illustrates the limitations in using high volume fractions.

We have measured the dependence of the coercivity and Curie temperature of nickel nanowire arrays as a function of wire diameter. Arrays of nickel nanowires with effective diameters from 30 nm to 200 nm have been fabricated by electrochemical deposition into mica templates. The nanowire density was systematically increased from 5×10^7 cm^{-2} for the 200 nm pores to 2×10^9 cm^{-2} for the 30 nm pores in order to maintain the same volume (area) fraction of nickel for all the samples. The relevant parameters are summarized

TABLE II Effective diameter (d), number density of tracks (n), and volume (area) fraction (f) of pores. $m(1)/n$, $m(2)/n$, and $m(3)/n$ represent the calculated fraction of pores derived from single, double, and triple tracks

d (nm)	n (# cm^{-2})	f	$m(1)/n$	$m(2)/n$	$m(3)/n$
500	1×10^7	0.0196	0.925	0.0363	0.000950
200	5×10^7	0.0157	0.939	0.0295	0.000617
150	1×10^8	0.0177	0.932	0.0330	0.000776
100	3×10^8	0.0236	0.910	0.0429	0.00135
75	5×10^8	0.0221	0.915	0.0404	0.00119
50	1×10^9	0.0196	0.925	0.0363	0.000950
33	2×10^9	0.0141	0.945	0.0267	0.000504

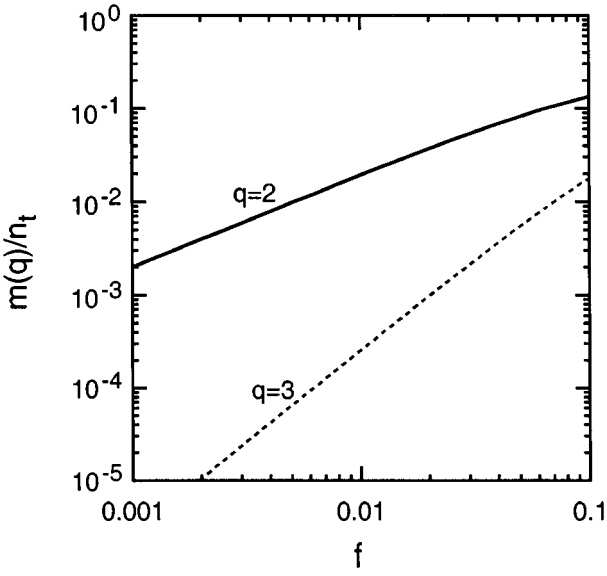

Figure 10 Calculated fractions of double ($q = 2$) and triple ($q = 3$) pores versus volume fraction.

in Table II. The calculated fractions of double and triple pores also remain the same for these samples at approximately 4% and 0.1% respectively. The values for the densities of overlapping pores were confirmed by analysis of a mica film with a track density of 3.1×10^6 cm^{-2} and relatively large pores ($d = 1.6 \pm 0.1\,\mu$m). In this case the calculated values for double and triple pores are 9.6% and 0.78%, respectively. Analysis of 220 pores revealed the fractional densities of double pores to be 8.2% and triple pores to be 0.91%, in good agreement with the predicted values.

Fig.11 shows typical hysteresis loops for a nickel nanowire array with an effective pore diameter of 100 nm obtained with the magnetic field applied parallel (//) and perpendicular ($\perp$) to the wire axes. The easy directions are along the wire axes, whereas the hard axes are perpendicular to the wires with a saturation field, due to the demagnetization field, of $2\pi M = 3.0$ kOe at room temperature. Fig.12a shows the size dependence of the coercivity (H_c) as a function of the effective wire diameter with the field applied parallel to the wires (perpendicular to the film). The measured coercivity increases with decreasing effective diameter, reaching a value of 800 Oe at an effective wire diameter of 30 nm. For smaller diameters, coercivities in excess of 1 kOe can readily be anticipated. These values are slightly larger than previous results for nickel nanowire arrays

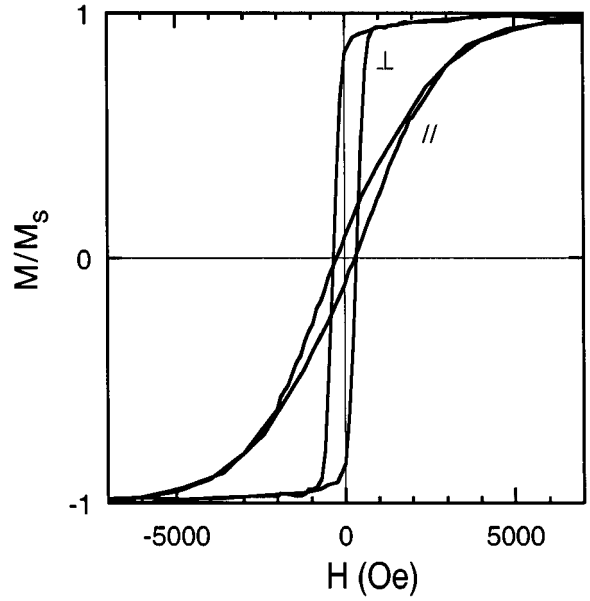

Figure 11 Hysteresis loops for a nickel nanowire array with an effective pore diameter of 100 nm obtained with the magnetic field applied parallel (//) and perpendicular ($\perp$) to the wires.

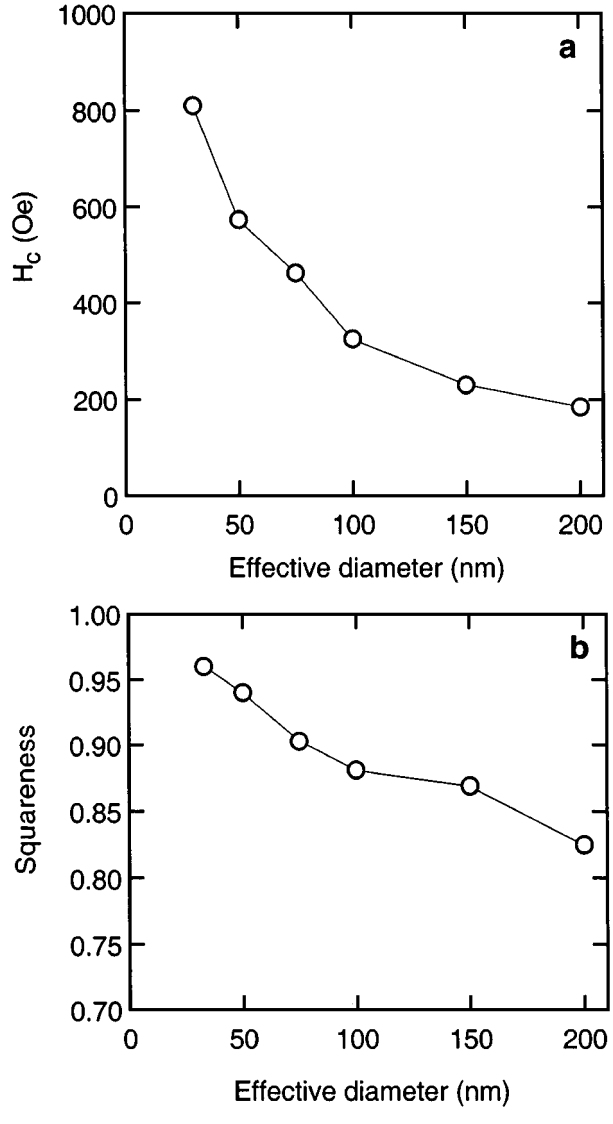

Figure 12 (a) Coercivity and (b) squareness of nickel nanowire arrays in single-crystal mica films as a function of the effective wire diameter.

in polycarbonate membranes [6] suggesting that the improved collimation and lower surface roughness of the pore surface play an important role in determining the properties of the nanowires.

Fig.12b shows the magnitude of the remanent magnetization obtained from the hysteresis loops and plotted as the squareness (SQ), defined as the ratio of remanence and saturation magnetization ($SQ = M_r/M_s$). The value of SQ is as high as 0.96 for the 30 nm diameter wires, decreasing gradually to 0.83 for the 200 nm diameter wires. The maximum value of 0.96 is significantly larger than the value of 0.90 obtained for 30 nm diameter wires in polycarbonate membranes [6–8]. Furthermore, the value of 0.83 for the 200 nm diameter wires is more than a factor of two larger than the value of 0.3 obtained for 200 nm wires in polycarbonate membranes. These enhancements can be attributed directly to the improved collimation of the pores, the uniform pore cross-section, and the low density of overlapping pores.

A significant advantage in using mica as a nanoporous template is its excellent thermal stability that allows measurement of high temperature magnetic phase transitions. Fig.13 shows normalized *M-T* curves for nickel nanowire arrays illustrating that the Curie temperature decreases with decreasing wire diameter. The Curie temperature, determined from the derivative of the *M-T* curves, is plotted versus wire diameter in Fig.14a illustrating a shift of 51 K for the 33 nm diameter nanowires. The Curie temperatures obtained by this method were independent of the applied magnetic field over the measured range 2,000 to 12,000 Oe.

The shift of the Curie temperature with decreasing diameter can be described by finite size scaling. The correlation length $\xi(T)$ of a magnetic system at temperatures close to the bulk transition temperature $T_c(\infty)$ exhibits asymptotic behavior described by:

$$\xi(T) = \xi_0 \left| 1 - \frac{T}{T_c(\infty)} \right|^{-\nu} \qquad (3)$$

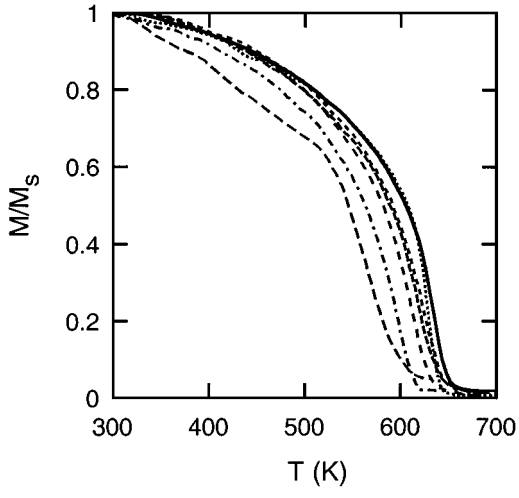

Figure 13 Normalized magnetization versus temperature for nickel nanowire arrays with diameters (from left to right) 33 nm, 50 nm, 100 nm, 150 nm, 200 nm, 500 nm, bulk nickel. The temperature was calibrated prior to each measurement using a bulk nickel sample and all measurements were obtained at $H = 2000$ Oe.

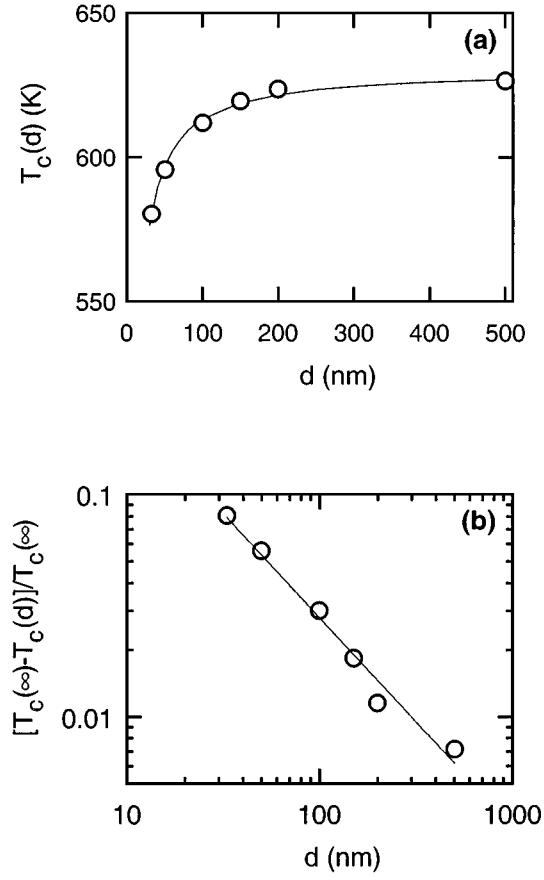

Figure 14 (a) Curie temperature $T_c(d)$ of nickel nanowire arrays versus wire diameter d. (b) log-log plot showing the reduced temperature $[T_c(\infty) - T_c(d)]/T_c(\infty)$ normalized to the Curie temperature for bulk Ni [$T_c(\infty) = 631$ K] versus wire diameter. The solid line corresponds to $\lambda = 0.94$ and $\xi_0 = 22$ Å.

where ξ_0 is the correlation length extrapolated to $T = 0$, and ν is the critical exponent for correlation [31]. For a magnetic system, such as a nanowire with diameter d, the growth of $\xi(T)$ will be limited by the wire diameter at d, resulting in a reduced Curie temperature defined by:

$$T_c(d) = T_c(\infty)\left[1 - \left(\frac{\xi_0}{d}\right)^{\lambda}\right] \qquad (4)$$

or

$$\frac{T_c(\infty) - T_c(d)}{T_c(\infty)} = \left(\frac{\xi_0}{d}\right)^{\lambda} \qquad (5)$$

where $T_c(d)$ is the Curie temperature for nanowires with diameter d, and $\lambda = 1/\nu$ is the shift exponent. Fig. 14b shows a log-log plot of the reduced temperature $[T_c(\infty) - T_c(d)]/T_c(\infty)$ versus wire diameter d, from which we obtain $\lambda = 0.94$ and $\xi_0 = 22$ Å.

Since the wire diameters are larger than the lattice spacing the nanowire are expected to behave as a constrained 3D system. However, the value of λ is lower than the theoretical values predicted by the 3D Heisenberg model ($\lambda = 1.4$) and the 3D Ising model ($\lambda = 1.58$) [32, 33]. The correlation length $\xi_0 = 22$ Å for the nickel nanowires is close to values of about 10 Å reported for ferromagnetic layers and about 20 Å obtained for antiferromagnetic CoO layers [33, 34].

4. Conclusions

Nanoporous, single-crystal mica films fabricated by nuclear track etching exhibit many unique properties and are excellent templates for electrochemical deposition of nanowire arrays. We have demonstrated that the improved collimation of the pores, the uniform pore cross-section, and the low density of overlapping pores results in enhancements in the magnetic anisotropy in comparison to other templates. Furthermore, the thermal stability of mica allows measurements of magnetic phase transitions that occur at elevated temperatures. The Curie temperature for nickel nanowire arrays is found to be reduced by as much as 51 K for the 30 nm diameter nanowires. The Curie temperature shift with wire diameter follows the finite-size scaling relation with $\lambda = 1.05 \pm 0.02$ and $\xi_0 = 36.9 \pm 3$ Å.

Acknowledgement

This work is supported by NSF MRSEC on Nanostructured Materials (Grant No. DMR 96-32526).

References

1. G. E. POSSIN, *Rev. Sci. Instrum.* **41** (1970) 772.
2. *Idem., Physica* **55** (1971) 339.
3. W. D. WILLIAMS and N. GIORDANO, *Rev. Sci. Instrum.* **55** (1984) 410.
4. J. T. MADSEN and N. GIORDANO, *Phys. Rev. B* **31** (1985) 6395.
5. C. R. MARTIN, *Science* **266** (1994) 1961.
6. T. M. WHITNEY, J. S. JIANG, P. C. SEARSON and C. L. CHIEN, *Science* **261** (1993) 1316.
7. L. PIRAUX, S. DUBOIS, E. FERAIN, R. LEGRAS, K. OUNADJELA, J. M. GEORGE, J. L. MAURICE and A. FERT, *J. Magn. Magn. Mater.* **165** (1997) 352.
8. R. FERRE, K. OUNADJELA, J. M. GEORGE, L. PIRAUX and S. DUBOIS, *Phys. Rev. B* **56** (1997) 14066.
9. L. SUN, P. C. SEARSON and C. L. CHIEN, *Appl. Phys. Lett.* **74** (1999) 2803.
10. L. PIRAUX, J. M. GEORGE, J. F. DESPRES, C. LEROY, E. FERAIN, R. LEGRAS, K. OUNADJELA and A. FERT, *ibid.* **65** (1994) 2484.
11. A. BLONDEL, J. P. MEIER, B. BOUDIN and J.-PH. ANSERMET, *ibid.* **65** (1994) 3019.
12. K. LIU, K. NAGODAWITHANA, P. C. SEARSON and C. L. CHIEN, *Phys. Rev. B* **57** (1995) 7381.
13. P. B. PRICE and R. M. WALKER, *J. Appl. Phys.* **33** (1962) 3400.
14. *Idem., ibid.* **33** (1962) 3407.
15. C. P. BEAN, M. V. DOYLE and G. ENTINE, *ibid.* **41** (1970) 1454.
16. R. L. FLEISCHER, P .B. PRICE and R. M. WALKER, "Nuclear Tracks in Solids" (University of California, Berkeley, 1975).
17. B. E. FISCHER and R SPOHR, *Rev. Mod. Phys.* **55** (1983) 907.
18. N. TSUYA, Y. SAITO, H. NAKAMURA, S. HAYANO, A. FURUGOHRI, K. OHTA, Y. WAKUI and T. TOKUSHIMA, *J. Mag. and Magnetic Materials* **54** (1986) 1681.
19. M. SAITO, M. KIRIHARA, T. TANIGUSHI and M. MIYAGI, *Appl. Phys. Lett.* **55** (1989) 607.
20. R. O'BARR, M. LEDERMAN and S. SCHULTZE, *J. Appl. Phys.* **79** (1996) 6101.
21. P.P. NGUYEN and R. J. TONNUCI, *Mater. Res. Soc. Symp. Proc.* **431** (1996) 421.
22. S. A. DURRANI and R. K. BULL, "Solid State Nuclear Track Detection" (Pergamon Press, 1987).
23. S. K. CHAKARVARTI and J. VETTER, *Nucl. Instrum. and Methods* **B62** (1991) 109.
24. G. GUILLOT and F. RONDELEZ, *J. Appl. Phys.* **52** (1981) 7155.
25. A. SIGRIST and R. BALZER, *Radiation Effects* **34** (1977) 75.
26. H. A. KHAN, N. A. KHAN and R. SPOHR, *Nucl. Instrum. Methods* **189** (1981) 577.
27. J. A. QUINN, J. L. ANDERSON, W. S. HO and W. J. PETZNY, *Biophysical Journal* **12** (1972) 990.
28. W. W. JACKSON and J. WEST, *Zeit. F. Krist.* **76** (1930) 211.
29. *Idem., ibid.* **85** (1933) 160.
30. W. L. BRAGG, "Atomic Structure of Minerals" (Cornell University Press, NY, 1937).
31. See for example H. E. STANLEY, "Introduction to Phase Transitions and Critical Phenomena" (Oxford University Press, New York, 1971) p. 46.
32. G. A. T. ALLAN, *Phys. Rev. B* **1** (1970) 352.
33. C. DOMB, *J. Phys. A* **6** (1973) 126.
34. T. AMBROSE and C. L. CHIEN, *Phys. Rev. Lett.* **76** (1995) 1743.
35. Y. LI and K. BABERSCHKE, *ibid.* **68** (1992) 1208.

Received 11 June
and accepted 19 August 1999